

Comparing ground magnetic field perturbations from global MHD simulations with magnetometer data for the 10 January 1997 magnetic storm event

X. Shao,¹ P. N. Guzdar,² G. M. Milikh,¹ K. Papadopoulos,¹ C. C. Goodrich,¹
A. Sharma,¹ M. J. Wiltberger,³ and J. G. Lyon³

Received 28 November 2000; revised 22 October 2001; accepted 24 October 2001; published 10 August 2002.

[1] A model has been developed to calculate the perturbed magnetic field at various ground-based magnetometer sites using the output of the ionospheric currents from the Lyon-Fedder-Mobarry Global MHD code. The model uses the computed ionospheric currents and the height dependence of the electrojet current above the ground, by evaluating the penetration depth of the precipitating energetic electrons, to calculate the perturbed magnetic field on the ground using Biot-Savart's law. By applying the model to the 10 January 1997 magnetic storm event we have calculated the perturbed magnetic field for four magnetometers and compared with observations. The comparison shows reasonable agreement between observations and simulations. The model including the dependence of the current sheet height on the precipitating electron energy reduces 10% error compared to the model with fixed current sheet height. The limitations of the global MHD model in calculating perturbed ground magnetic field are also discussed. *INDEX TERMS:* 2788 Magnetospheric Physics: Storms and substorms; 2736 Magnetospheric Physics: Magnetosphere/ionosphere interactions; 2753 Magnetospheric Physics: Numerical modeling; 2475 Ionosphere: Polar cap ionosphere; *KEYWORDS:* global MHD simulation, magnetosphere-ionosphere coupling, magnetometer, magnetospheric storms

1. Introduction

[2] On 10 January 1997 a magnetic cloud produced a major geomagnetic storm. This storm was the first solar terrestrial disturbance whose temporal development was followed from its solar source and its subsequent effects on the magnetosphere and ionosphere using the entire suite of resources of the International Solar Terrestrial Physics (ISTP) program. The SOHO Large-Angle Spectrometric Coronagraph (LASCO) experiment observed the CME expanding from the solar surface apparently toward the Earth on January 6. Early on January 10, WIND first observed the (CME associated) magnetic cloud, which produced a complex magnetic storm lasting 22 hours.

[3] Global MHD simulations that include ionospheric response and are dynamically driven by upstream satellite data allow for direct comparison with the field and flow quantities measured by detectors on magnetospheric satellites, ground-based instruments and images from the Polar satellite. Using the Lyon-Fedder-Mobarry (LFM) Global magnetohydrodynamic (MHD) simulations, the group at

Maryland (Goodrich, Wiltberger, Lopez, and Papadopoulos) in collaboration with J. Lyon from Dartmouth College, simulated the 10–11 January 1997 storm event. The simulation was initialized using upstream Wind satellite data. Forty-eight hours of real-time development of the geomagnetic activity in the magnetosphere and ionosphere were simulated. The results of the three-dimensional (3-D) MHD simulation of this event and its consequence on the magnetosphere and ionosphere have been presented by Goodrich *et al.* [1998a, 1998b], Papadopoulos *et al.* [1999], and Lopez *et al.* [1999]. The simulation results agreed well with ground-based and geosynchronous satellite observations. They showed that during the period of southward interplanetary magnetic field (IMF) the ionospheric activity was strongly correlated with the solar wind density variation. It was concluded that both the solar wind magnetic field and ram pressure are important in determining the structure of the magnetosphere and the activity in the ionosphere during the 10–11 January 1997 magnetic storm. In the present work we have used the time history of the ionospheric currents computed by the ionosphere module of the LFM code to develop a model for calculating the time history of the perturbed magnetic field at various ground-based locations to compare with magnetometer data.

[4] We first briefly outline some relevant parts of the code that facilitate the understanding of our model. In the LFM Global MHD model [Fedder *et al.*, 1995b], at the inner boundary located at 2–3 R_E from the Earth, the parallel current density J_{\parallel} is computed at each instant of time. This parallel current is mapped into the ionosphere along unper-

¹Department of Astronomy, University of Maryland, College Park, Maryland, USA.

²Institute for Plasma Research, University of Maryland, College Park, Maryland, USA.

³Department of Physics, Dartmouth College, Hanover, New Hampshire, USA.

turbed dipole magnetic field lines. The height-integrated current continuity equation yields the perpendicular current density (both Hall and Pedersen) in the ionosphere. By using semiempirical models for the conductances the electrostatic potential is computed. The contours of constant electrostatic potential are streamlines of flow in the ionosphere. The ionospheric solution for electric field is mapped back to the inner boundary of the MHD model and is used to define the boundary condition for the plasma velocity via $\vec{E} \times \vec{B}$ velocity. *Kisabeth and Rostoker* [1977] showed how three-dimensional current systems associated with magnetospheric substorms can be used to quantitatively evaluate the magnetic field perturbation at any location on the ground. In this paper, following a similar approach using the Biot-Savart law, we model the perturbations of magnetic field produced at various locations by the 2-D ionospheric current system. One important novel feature of our model is to evaluate the instantaneous height of the 2-D current system by using the energy of the precipitating electrons to calculate the penetration depth and hence the position of the auroral electrojet.

[5] Using Fukushima's theorem [*Fukushima*, 1976], *Raeder et al.* [2001] reduce the three-dimensional Biot-Savart integration to a two-dimensional integration over the ionospheric toroidal (equivalent) current. Under the assumption that the ground magnetic field perturbation produced by the field-aligned current and by the poloidal part of the ionospheric current cancel, the ground magnetic field perturbation can be obtained by applying Biot-Savart's law with ionospheric toroidal current [*Raeder et al.*, 2001]. In our current model the ground magnetic perturbations are calculated by applying Biot-Savart's law with the ionospheric shell current. The contribution to the ground magnetic field perturbations from the field-aligned current is neglected. The instantaneous height of ionospheric current sheet at each grid point is calculated from the energy of the precipitating electrons and incorporated into Biot-Savart's law. This will reduce error compared to the model using fixed current sheet height. Another difference between our work and the works by M. Wiltberger et al. (Results from the Lyon-Fedder-Mobarry global magnetospheric model for the electrojet challenge, submitted to *Journal of Geophysical Research*, 2001; hereinafter referred to as submitted manuscript, 2001) and *Raeder et al.* [2001] is that, for the magnetic storm event studied in this paper, the ground magnetic field perturbations are produced by solar wind density pulses during a long period of strong southward IMF. While in the works of Wiltberger et al. (submitted manuscript, 2001) and *Raeder et al.* [2001], the ground magnetic field perturbations are produced from a typical magnetic substorm event due to the southward turning of the solar wind IMF and the evolution tracks the growth phase, expansion phase, and recovery phase. For the event studied in this paper, under long period of strong southward IMF, in responding to the solar wind density pulse, the ground magnetometers show large perturbations of magnetic field (600 to 1500 nT). The long-period envelop of these large-amplitude perturbations can be directly related to the increase of solar wind ram pressure. There are also large-amplitude spikes of period 10 to 15 min in oscillatory format added on top of the envelop. The model presented in this paper can reproduce

the long-period envelop of the ground magnetic field perturbations with smaller amplitude. These long-period baseline perturbations can be attributed to the perturbations in the ionosphere current flowing within the two-cell convection system. However, our model could not reproduce the large-amplitude spikes of 10–15 min duration.

[6] In the following section, we will first very briefly describe the global MHD model we used in our simulations. Next, the ionosphere module used with the MHD code is discussed. Then, using the Biot-Savart's law, the model for computing the perturbations of ground magnetic field is developed. Here we will also show how the electron energy dependence of the ionospheric auroral electrojet height is calculated. In section 3, the general response of the ionosphere electric potential for the 10 January 1997 magnetic storm event will be described. Then, with the model we have developed, the perturbations of the magnetic field at four ground stations will be presented and compared with magnetometer observations. Finally, we summarize our work.

2. Simulation Models

2.1. The Lyon-Fedder-Mobarry Code

[7] The Lyon-Fedder-Mobarry (LFM) 3-D MHD simulation code [*Fedder and Lyon*, 1987; *Fedder et al.*, 1995a, 1995b; *Mobarry et al.*, 1996] models the solar wind, the magnetosphere beyond 2–3 R_E and the coupling of the MHD solutions to an electrostatic model for the ionosphere. The code solves the MHD equations within a large cylindrical region 50 R_E in radius and 360 R_E long [*Goodrich et al.*, 1998a]. The front inflow boundary is at $x = 30 R_E$. The inner boundary is at $(x^2 + y^2 + z^2) = 2 R_E^2$, where x , y , z are the solar magnetospheric coordinates. The simulation was performed in the Solar Magnetic (SM) coordinate system allowing for the tilt of the Earth's magnetic dipole relative to the solar wind flow direction to be included. Outflow conditions are imposed on the downstream boundary. Elsewhere, external boundary conditions were specified using Wind solar wind data propagated appropriately to the front and cylindrical sides of the grid. The propagation of the Wind solar wind data to the front side of the grid in the LFM model is described in detail by [*Wiltberger et al.*, 2000]. In general, the structure of Faraday's law for ideal MHD prevents advection of components of the magnetic field that are not transverse to the flow direction. We assume $B_X(t) = a + bB_Y(t) + cB_Z(t)$, where a is in nanoteslas and b and c are scalars without dimension. Then we have effectively created a new normal direction $\vec{n} = \lambda(\vec{i}_b - \vec{j}_c - \vec{k})$ along which the normal magnetic field is constant. Here, $\lambda = 1/\sqrt{1 + b^2 + c^2}$ is a scaling factor. This allows a time dependent B_X to be introduced into the simulation by sweeping updates of the solar wind parameters across the front boundary. For the 10 January 1997 magnetic storm event, the simulation was run with $a = -4.38$ nT, $b = 0.0916$, $c = 0.4486$.

[8] We discuss the ionosphere module in more detail since it is relevant to our present studies. In the LFM Global MHD model [*Fedder et al.*, 1995b; *Slinker et al.*, 1999], at the inner boundary located at 2 R_E from the Earth, the parallel current density J_{\parallel} is computed at each instant of time. This parallel current is mapped into the

ionosphere along unperturbed dipole magnetic field lines. The height-integrated current continuity equation yields the perpendicular current density (both Hall and Pedersen) in the ionosphere. By using semiempirical models for the conductances [Robinson *et al.*, 1987], the electrostatic potential is computed. The basic 2-D current continuity equation is

$$\nabla_{\perp} \Sigma \nabla_{\perp} \Phi = J_{\parallel}, \quad (1)$$

with Φ the ionospheric potential, Σ the height-integrated anisotropic conductivity tensor, and J_{\parallel} the field-aligned current. The conductance tensor has both Pedersen and Hall components, whose values consist of two contributions. The first contribution is from the steady solar EUV flux and the second contribution is due to the particle precipitation in the auroral region. The latter contribution is from the empirical model developed by Robinson *et al.* [1987]. The detailed empirical model for calculating the anisotropic conductance tensor in LFM was presented in [Fedder *et al.*, 1995b]. Here, we restate the calculation briefly since some equations will be referred to in section 4.

[9] According to Robinson *et al.* [1987], the auroral contributions to the Pedersen and Hall conductivities can be calculated using the empirical method:

$$\delta\Sigma_P = 1.0 \times 10^{-4} \times \frac{E^3 \phi^{\frac{1}{2}}}{1 + 0.0625E^2} \quad (2)$$

$$\delta\Sigma_H = 0.45E^{0.85} \delta\Sigma_P, \quad (3)$$

where E and ϕ are the energy and flux of the precipitating electrons. E is in keV; ϕ is in $1/\text{cm}^2\text{s}$, and $\delta\Sigma_P$ and $\delta\Sigma_H$ are in mhos. Note that equations (2) and (3) are dimensionally different from that used by Robinson *et al.* [1987].

[10] The energy and flux of precipitating electrons in the LFM are determined from the MHD quantities within the inner most grid cells. First, a provisional set of energy, E_o and flux, ϕ_o , values are determined from sound speed, c_s , and density, ρ using

$$E_o = \alpha c_s^2 \quad (4)$$

$$\phi_o = \beta \rho E_o^{\frac{1}{2}}, \quad (5)$$

where c_s is the sound speed at the inner boundary of the magnetosphere. Typically, it is over 100 km/s as it corresponds to the plasma temperature in the plasma sheet. The parameters α and β are chosen constants that map the magnetospheric plasma thermal flux and energy from the MHD inner boundary to the inner ionosphere. In our simulation, $\alpha = 1.25 \times 10^{-15}$ given that E_o is in keV and c_s is in cm/s; $\beta = 2.0 \times 10^{29}$ given that ρ is in g/cm^3 and ϕ_o is in $1/\text{cm}^2\text{s}$.

[11] The field-aligned electric potential energy between the ionosphere and the innermost MHD mesh cell boundary is defined as

$$E_{\parallel}(\text{keV}) = \frac{Rj_{\parallel}|E_o^{\frac{1}{2}}}{\rho}. \quad (6)$$

Here, j_{\parallel} is the field-aligned current in the inner MHD mesh cells and R is a scaling factor for the potential drop and includes an ‘‘effective resistivity’’ to field-aligned current. In our simulation, with j_{\parallel} in A/m^2 , ρ in g/cm^3 , and E_o in keV, the factor R is taken to be 1.88×10^{-17} for the current out of the ionosphere and $R = 3.76 \times 10^{-18}$ for the current into the ionosphere.

[12] The flux of precipitating electrons is modified to include the effects of field-aligned potential drops and geomagnetic mirroring. It’s defined as

$$\phi = \phi_o \left(8 - 7 \exp^{-\frac{E_{\parallel}}{7E_o}} \right) \quad E_{\parallel} > 0 \quad (7)$$

$$\phi = \phi_o \exp^{\frac{E_{\parallel}}{7E_o}}, \quad E_{\parallel} < 0. \quad (8)$$

While the energy of precipitating electrons is simply

$$E = E_o + E_{\parallel}. \quad (9)$$

The total ionospheric conductance is taken as the square root of the sum of the squares of the EUV conductance and the auroral conductance. The 2-D height integrated ionospheric current density is

$$\vec{J}_{\perp} = \Sigma \nabla_{\perp} \Phi. \quad (10)$$

For the calculation presented in this paper, the three parameters α , β , and R are supposed to be given and kept constant. The ground magnetic field perturbations are calculated from the ionospheric current density and the energy of precipitating electrons that are available from the simulation.

2.2. Modeling Perturbed Magnetic Field

[13] The perpendicular current obtained from equation (10), is specified on a spherical shell with an angular range from 45 degrees to 90 deg in latitude (solar-magnetosphere coordinate) for each hemisphere. The contributions from the field aligned current to the ground magnetic field perturbations are not included. To calculate the perturbed magnetic field produced by the ionospheric current, we implement the generalized form of Biot-Savart’s law [Kisabeth and Ros-toker, 1977]

$$\vec{B}(\vec{r}_0) = \mu_o/4\pi \int_s \frac{\vec{J}(\vec{r}(\epsilon)) \times (\vec{r}_0 - \vec{r}(\epsilon)) d^2\vec{r}(\epsilon)}{|\vec{r}_0 - \vec{r}(\epsilon)|^3}. \quad (11)$$

Since the ionospheric current in our case is 2-D ($\vec{J}(\vec{r})$ has been height integrated over the thickness of the current sheet), the integral is calculated on the spherical shell $d^2\vec{r}$ of the current sheet. Here, \vec{r}_0 is the position of the station site in SM coordinates, where the perturbed magnetic field is computed and $\vec{r}(\epsilon)$ denotes the position of the ionospheric current sheet in SM coordinates. The height of the ionospheric electrojet changes in time and is determined by the energy of the precipitating electrons. The precipitating energetic electrons ionize the neutrals and are finally stopped when they lose all their energy in the ionization process. The more energetic the electrons are, the

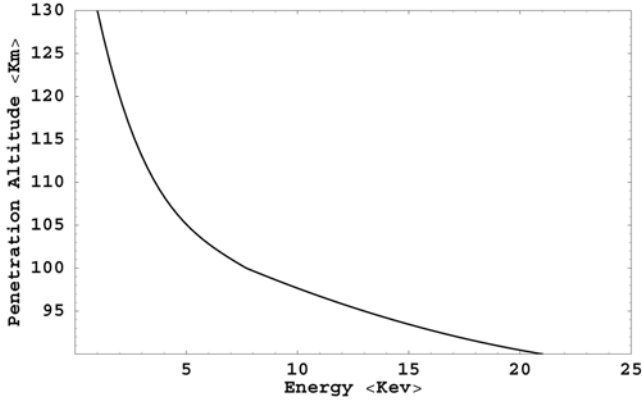


Figure 1. The electron penetration altitude versus electron energy (computed from our model).

deeper they penetrate into the atmosphere. Thus $\vec{r}(\varepsilon)$ can be expressed as

$$|r(\varepsilon)| = R_E + h(\varepsilon). \quad (12)$$

Here R_E is the radius of the Earth and $h(\varepsilon)$ is the energy-dependent height of the electrojet current. From the LFM code we get a time history of the energy of the precipitating electrons at each grid point. Knowing the instantaneous energy of the precipitating electrons we can now calculate the desired height of the 2-D electrojet current sheet at each grid point.

[14] According to [Milikh *et al.*, 2001], the energy balance of electrons flowing downward along the field lines and ionizing the neutral atmosphere is given by

$$\frac{d\varepsilon}{dz} = -\sigma_{ion}(\varepsilon)\varepsilon_{ion}N_n(z), \quad (13)$$

where σ_{ion} (in cm^2) is the ionization cross section, while ε_{ion} is the energy loss per ionization, which is typically 35 eV [Rees, 1989] and N_n is the neutral density. In an exponential atmosphere $N_n \sim e^{-z/L}$ where L is the density scale height. Here, we take $L = 10$ km. The ionization cross section of air by electrons in the energy range $\varepsilon < 20$ KeV is described with sufficient accuracy by the following interpolation formula [Gurevich *et al.*, 1997]

$$\sigma_{ion}(cm^2) \simeq 8.3 \times 10^{-16} \frac{\varepsilon/\varepsilon_m - 0.11}{1 + 1.85(\varepsilon/\varepsilon_m)^{1.75}}, \quad (14)$$

where $\varepsilon_m = 110$ eV corresponds to the peak of σ_{ion} .

[15] By substituting equation (14) into equation (13) and integrating while taking into account that in the energy range provided by the LFM model, 1000 eV $\leq \varepsilon \leq 20000$ eV, $\varepsilon/\varepsilon_m \gg 1$, we find that the air density at the penetration altitude (z_p) is

$$N_n(z_p) = \frac{4 \times 10^9 cm^{-3}}{(L/10km)} \left(\frac{\varepsilon}{\varepsilon_m}\right)^{1.75}, \quad (15)$$

where ε is in eV.

[16] Using the U.S. Standard Atmosphere (1976), we have computed the penetration altitude z_p for different electron energies ε . The resulting dependence of penetration altitude z_p on energy ε is plotted in Figure 1. After penetration altitude z_p is obtained, the energy-dependent height of the electrojet current $h(\varepsilon)$ is calculated as $h(\varepsilon) = z_p + \delta z/2$, where δz is the thickness of the ionization layer and can be approximated as $\delta z = L = 10$ km.

[17] Thus knowing the height dependence and the current density of the electrojet we can use equation (11) to compute the magnetic field at any location $\vec{B}(\vec{r}_0)$ in the SM coordinate system as a function of time. The integral is discretized into a summation over all the grid points. Figure 2 shows the grid configuration. Figure 2 The nonuniform grids of the global MHD model have been mapped into the uniform grids in polar coordinate as shown in Figure 2. The adjacent longitudinal ($j, j \pm 1$) and azimuthal ($i, i \pm 1$) lines are two degrees apart, respectively. The longitudinal lines ($j, j \pm 1$) converge at the northern pole. The points ($i \pm 1/2, j \pm 1/2$), and ($i \pm 1/2, j \mp 1/2$) are at the center of each grid. For grid point (i, j), its contribution to the integral is calculated within the area formed by the dotted lines. We assume same current sheet height and uniform horizontal current inside the area formed by the dotted lines. The integration is evaluated by summing over all the grid points.

[18] We then calculate the magnetic field in the local observational coordinate system ($\hat{r}_0, \hat{\theta}, \hat{\phi}_0$) of the desired station as $\vec{B}(\vec{r}_0) = B_1\hat{r}_0 + B_2\hat{\theta} + B_3\hat{\phi}_0 = -Z\hat{r}_0 - H\hat{\theta} + D\hat{\phi}_0$. Here, H is the component that points toward the north magnetic pole, D points eastward and Z points down toward the center of the Earth. Finally, to account for the contribution from the current induced in the ground, the calculated magnetic field is enhanced by a factor of 2. The factor of 2 is justified if the earth surface is treated as an infinite conductor, which is valid for processes, which have a slow timescale variation. For MHD timescales this is particularly justified. We hasten to add that the individual component of the magnetic field will be strongly influenced by the

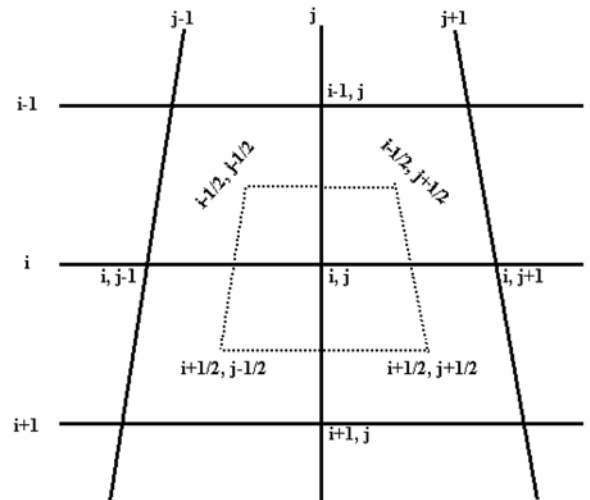


Figure 2. The grid configuration for the model.

local conductivity of the ground and that would rotate the polarization of the magnetic field. Thus we have focused on comparing the magnitude of the horizontal component ($\sqrt{H^2 + D^2}$), the Z component and the total field ($\sqrt{H^2 + D^2 + Z^2}$) with ground-based magnetometer data.

3. Simulation Results for 10 January 1997 Magnetic Storm Event

[19] In this section we compare the time history of the perturbed horizontal, Z and total magnetic field computed using equation (11), to the data from four high-latitude magnetometers. The time period we investigated was from 0600 to 1300 UT on 10 January 1997. During this interval the interplanetary magnetic field in the solar wind was mainly southward and quite steady. The ionospheric activity was strongly correlated with the solar wind density variation. Figure 3 shows the solar wind condition observed by the Wind satellite. Figure 3 All the vector components are in GSM coordinates. V_y and V_z are not plotted because they are in the range of -50 to 50 km/s. The solar wind velocity is quite steady for the time interval of interest. The solar wind experienced a density increase between 0630 and 0830 UT. There was another large solar wind density pulse around 1030 UT. Owing to the time delay for the solar wind to arrive at the magnetopause from the Wind satellite, and subsequent propagation into the magnetosphere, the two major perturbations observed in the ionosphere triggered by the density pulses occurred in the interval between 0700 and 0900 UT and around 1100 UT.

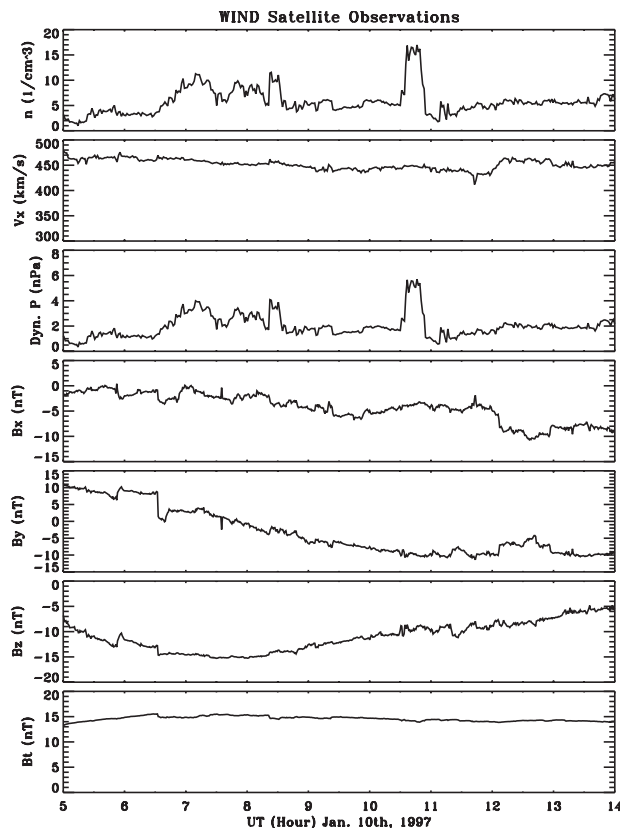


Figure 3. Solar wind condition as observed by the Wind satellite on 10 January 1997.

Table 1. Magnetometer Site Coordinates

	Geographic Coordinates		Magnetic Coordinates	
	Latitude	Longitude	Latitude	Longitude
Sondre Strom (Greenland)	N67.02	E309.28	N73.35	E41.48
Rankin Inlet (Canada)	N62.82	E267.89	N70.37	E338.92
Iqaluit (Canada)	N63.75	E291.57	N72.09	E14.53
Gakona (Alaska)	N62.41	E214.88	N63.12	E267.25

[20] The geographic and magnetic coordinates for the four magnetometers stations used in our comparison are listed in Table 1.

[21] Figure 4 shows the northern polar cap potential contour plots obtained from the simulation. The interval between two adjacent potential contours is 25 kV. Solid lines depict the positive potential, and dashed lines depict the negative potential. Since the interplanetary magnetic field is southward, the ionospheric potential contour plots show the characteristic two-cell pattern. Four snap shots are picked to present the typical behavior of the ionosphere. In each panel the four magnetometer sites are marked with four symbols, respectively. The labels below the plots identify each symbol with one of the four stations. Here, we note that the electric potential calculated from the global MHD model is ~ 2 to 2.5 times larger than the value derived from semi-empirical models during the time interval we are interested. The discussions about this discrepancy are given in section 4.

[22] In Figure 4, at 0605 UT, as a result of long period of southward IMF, the two-cell pattern in the ionosphere is fully developed. The cross-polar cap electric potential (maximum-minimum) is ~ 270 kV. At 0804 UT the perturbation caused by the increase of the solar wind density arrives in the ionosphere. The magnitude of electric potential is enhanced significantly. The cross-polar cap potential reaches ~ 375 kV. The enhancement of the ionospheric electric potential lasts until 0930 UT. At 0956 UT the ionospheric electric potential recovers from the perturbation. During this time period, the solar wind conditions are roughly steady for ~ 1 hour. The large-density pulse observed by Wind satellite at ~ 1030 UT has its effects in ionosphere at ~ 1100 UT. The panel for 1102 UT shows the corresponding enhancement of the ionospheric potential. For the four magnetometer sites, Gakona is at low SM latitude and remains mainly on the night side sampling the overhead current associated with the negative potential cell and subsequently the positive cell. Also, during the entire period this station is at the boundary of the auroral oval. On the other hand, Sondre Strom, Iqaluit, and Rankin Inlet sample the current mainly inside the positive potential cell.

[23] Applying the model developed in section 2.2, we calculate the magnetic field perturbations for the four magnetometer sites. Figure 5 shows the precipitating electron energy calculated from the global MHD model at sites right above the four locations. The precipitating electron energy is less than 20 keV. The time interval when the increase of precipitating electron energy occurs is well correlated to the period when the solar wind density pulse occurs. The derived penetration altitude above the four locations is presented in Figure 6. During quiet time the penetration altitude is around 130 km and during active time interval, the penetration altitude is around 100 km.

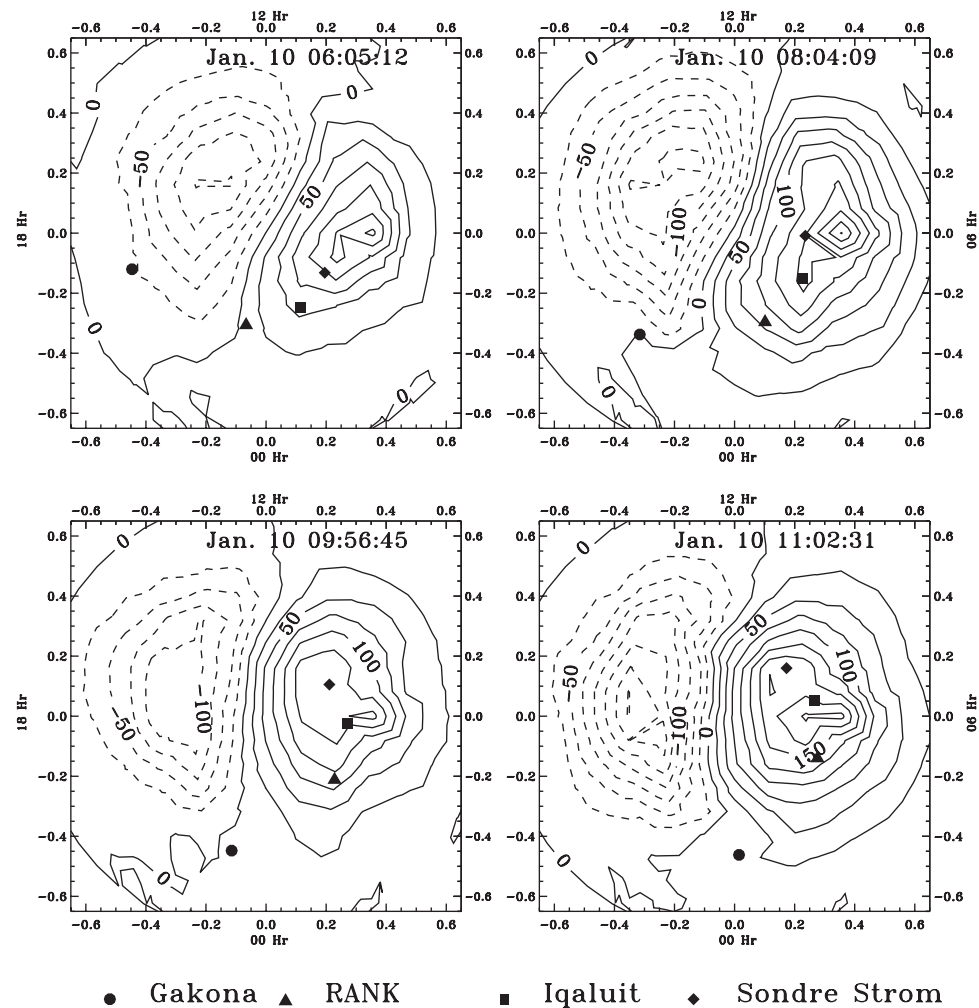


Figure 4. Northern polar cap electric potential contours for four time instants from the simulation. Each adjacent contour is 25 kV apart. Solid lines depict the positive potential, and dashed lines depict the negative potential. In each panel, the four magnetometer sites are marked with four symbols, respectively. The time for each panel is labeled on top part of the panel. The labels below the plots identify each symbol with one of the four stations. RANK denotes the station at Rankin Inlet.

[24] Figures 7, 8, 9, and 10 show the comparisons of the magnitude of the horizontal component ($\sqrt{H^2 + D^2}$), the Z component and the total perturbed magnetic field ($\sqrt{H^2 + D^2 + Z^2}$) (all in nanoteslas) between observations and simulations for the four different locations. In each of these figures we show the time history of the magnetometer data (solid line), the numerically computed data with fixed electrojet current sheet height (dashed line) and the numerically computed data with the height-dependence included (dotted line). The original simulated results for Gakona lagged behind the observations for ~ 15 min. We searched inside the $400 \text{ km} \times 400 \text{ km}$ grid cell, and Figure 10 presents the closest match.

[25] For Sondre Strom, Iqaluit, and Rankin Inlet the simulation results are in reasonable agreement with observations for the temporal behavior of both the horizontal and the total perturbed magnetic field. The two density perturbations which induce events that occurred between 0700 and 0900 UT and around 1100 UT are captured at these three sites. However, the calculated magnitude is smaller for

these perturbations, especially around 1100 UT. We speculate that two factors contribute to the underestimation of the perturbed magnetic field. The first factor is that due to the lack of a realistic ring current model, the region 2 model current is not well developed and the modeled ground magnetic field perturbations is small. In other words, the direct effects of the density pulse in the solar wind on the magnetosphere are on the day side reconnection, the compression of the magnetosphere and the tail lobe reconnection. All of these will contribute to enhance the field-aligned current which feeds into ionosphere. This is simulated by the global MHD model. The region 2 current is expected to be enhanced and be closed with ring current in the magnetosphere. However, in global MHD model the ring current is not included and region 2 current is not fully developed. Therefore the modeled total ionospheric current is not large enough to produce the observed magnitude of the perturbations. Another factor contributing to the underestimation is the neglecting of two-fluid effects in the global MHD model. During the expansion phase, strong dipolarization

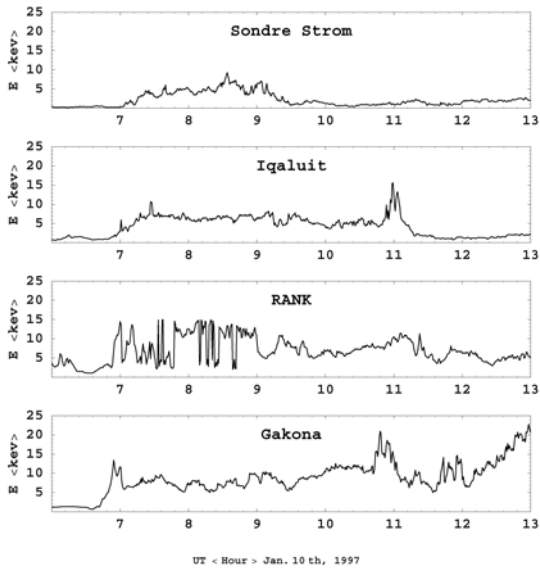


Figure 5. Time history of precipitating electron energy as simulated right above the four stations. RANK denotes the station at Rankin Inlet.

of the stretched field lines occurs on the nightside of the magnetosphere. The field lines that move rapidly toward the Earth carry the plasma with them. These processes can be well represented by the MHD model. However, in the inner tail where the electrons drift in the gradient of \mathbf{B} direction dominates, a strong polarization electric field develops because of the large difference in the Larmor orbits of the electrons and ions. This electric field maps into the ionosphere, giving rise to the westward drift of the ionospheric plasma. Since the production of the polarization field is

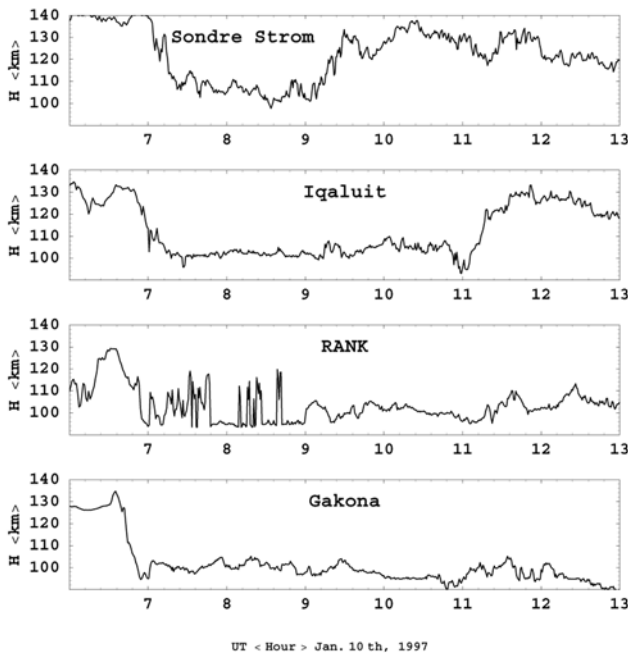


Figure 6. Time history of penetration altitude as simulated right above the four stations. RANK denotes the station at Rankin Inlet.

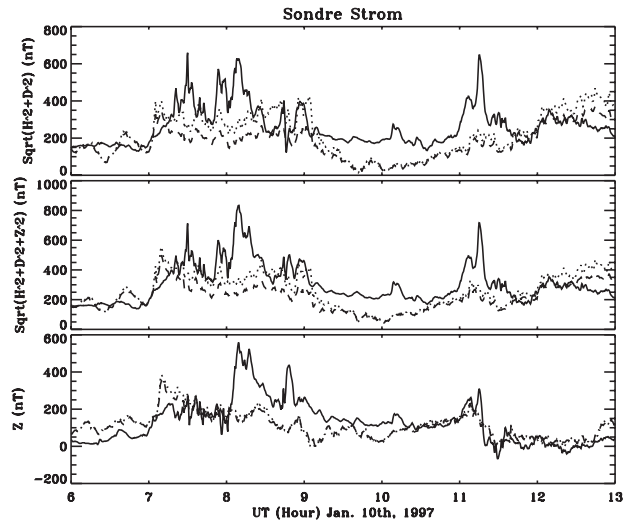


Figure 7. Comparison of the horizontal, total, and Z component perturbed magnetic field between simulations and observations for Sondre Strom. The solid curve is from observations, the dotted curve is from simulation with current sheet height-dependent model, and the dashed curve is from simulation with fixed height model.

strictly a two-fluid effect. Thus the MHD model underestimates the westward drift flow.

[26] For the Z component the model can only capture the average trend of variation for Sondre Strom, Iqaluit, and Rankin Inlet. The simulated Z component misses the variations shown in the observation for the time interval 0700 to 0900 UT. It captures some signatures of the variation that occurred around 1100 UT. The comparison for Z component magnetic field does not seem to be as good as that for $(\sqrt{H^2 + D^2})$ and $(\sqrt{H^2 + D^2 + Z^2})$. This is because that the calculation of the Z component magnetic field is affected more by the limited resolution of the ionosphere model than the horizontal component of the magnetic field. In our calculation the current in the overhead grid cell produces mainly horizontal magnetic field perturbations. The Z com-

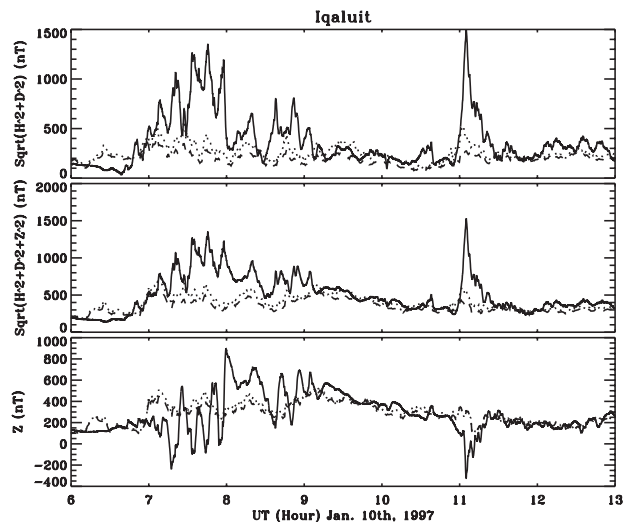


Figure 8. Similar comparison as in Figure 8 for Iqaluit.

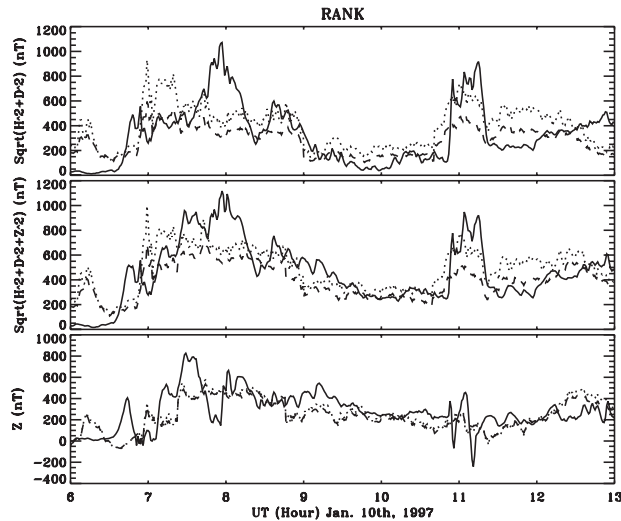


Figure 9. Similar comparison as in Figure 8 for Rankin Inlet.

ponent magnetic field is produced by the ionospheric currents in the grid cells that are farther away from the ground station. With current resolution of grid size $400 \text{ km} \times 400 \text{ km}$, assuming uniform current in the overhead grid smooths the current and excludes any localized feature which may contribute to the perturbation of the Z component magnetic field.

[27] There are fine structures of duration 10–15 min in the magnetometer data. These spikes are of large magnitude. Global MHD simulation is unable to capture these features. We speculate that they could be produced by local auroral arcs, which are not present in the global MHD ionospheric model. Besides this, some mismatch in the timing between the model and observations is apparent. The agreement is poor for Gakona, which is located at a low SM latitude ($N63.12$). The observed large perturbations occurring around 1100 UT is totally missed. We speculate that it is produced by local auroral arc. Our calculations show that a perturbation occurs around 1140 UT. This is the simulated

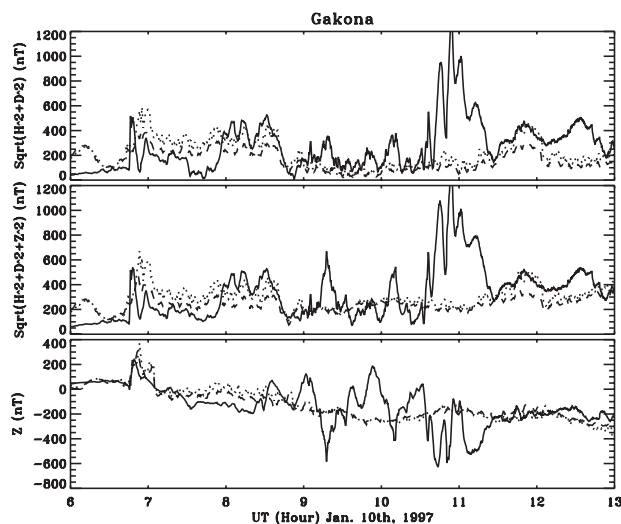


Figure 10. Similar comparison as in Figure 8 for Gakona.

Table 2. Root-Mean-Square Error Ratio Between Height-Dependent Model and Fixed-Height Model for the Horizontal, the z Component and the Total Ground Magnetic Field Perturbations

Ground Station	$\sqrt{H^2 + D^2}$	$\sqrt{H^2 + D^2 + Z^2}$	Z
Sondre Strom	0.88	0.86	0.99
Rankin Inlet	1.02	0.97	0.99
Iqaluit	0.84	0.83	1.00
Gakona	0.94	0.97	1.05

response to the second solar wind density pulse at Gakona. Gakona is near the lower boundary of the ionospheric model and the nonuniform grid size is larger compared to that at high latitude (see Figure 2). Thus the reduced resolution and boundary condition leads to worsening the comparison between the observed magnetometer data and the calculated data.

[28] In order to compare the performances of the model including height dependence of the current layer to the model with a fixed current sheet height, we define the root mean square error (RMSE) as the error measure of our prediction.

$$\text{RMSE} = \sqrt{\frac{\sum (X_{\text{simu.}} - X_{\text{observ.}})^2}{N}} \quad (16)$$

Here, X is the one of the components of the ground magnetic field perturbations. N is the data points in the interval from 0600 to 1300 UT on 10 January 1997. The resulting error ratio between these two models is tabulated in Table 2.

[29] For Sondre Strom and Iqaluit the inclusion of the height dependence improves the comparison with the ground data for horizontal and total magnetic field. The error ratio is reduced by more than 10%. For Z component, including height dependence doesn't improve the prediction. In our calculation, the Z component of the ground magnetic field perturbation is produced by the grids that are not right above the station and their distance to the ground station is less affected by the current sheet height. For Rankin Inlet we note that the poor performance of the height-dependent model mainly appears after 1130 UT. However, neither of the models compares well with observations after 1130 UT. If we change the time interval to from 0600 to 1130 UT to calculate the error ratio, then the error ratio between the height-dependent model and the height-fixed model for Rankin Inlet is 0.98 for the ($\sqrt{H^2 + D^2}$) component, 0.89 for the total magnetic field, and 0.96 for the Z component. The error is reduced by 10% with the height-dependent model for the total magnetic field. For Gakona the comparison itself is poor, we do not expect the height-dependent model to improve the results.

4. Discussion

[30] The electric potential presented in Figure 4, which is calculated from the global MHD model, is ~ 2 to 2.5 times larger than the value derived from semiempirical models during the time interval we are interested. The semiempirical models are the assimilative mapping of ionospheric electrodynamic (AMIE) technique [Lu et al., 1998] and the

Wiemer ionospheric convection model [Jordanova *et al.*, 1999]. Both of the semiempirical models are derived from observations of many ground stations and both show large cross polar cap potential (110 to 200 kV) during the time interval between 0600 and 13:00 UT on 10 January 1997. While our simulated peak cross polar cap potential is around 400 kV and for the whole time interval the average cross polar cap potential is around 270 kV. The relative magnitude change of the cross-polar cap potential simulated from our model, which is a 40–50 percent increase during the active period for the Northern Hemisphere, is about the same as that from the Weimer model. After comparing the derived Hall conductance from observations at Sonder Strom with our simulation, we found that the conductance derived from our model is ~ 2 – 2.5 times less than the observations. Because of this, the horizontal ionospheric current which comes mainly from Hall current still has a reasonable value. Actually, the ionospheric model in the global MHD model originates from the current continuity equation that states that the field aligned currents, J_{\parallel} , must be closed by the divergence of ionospheric current, namely $\nabla \cdot J_{\perp} = J_{\parallel}$, where J_{\perp} is the height-integrated perpendicular current. Therefore the ionospheric shell current J_{\perp} is of reasonable magnitude as long as the simulated J_{\parallel} in the magnetospheric model is reasonable. As shown in section 3, the ground magnetic field perturbations derived from J_{\perp} are of reasonable magnitude compared to observations.

[31] Winglee *et al.* [1997] studied the global characteristics of the auroral oval during the Geospace Environment Modeling (GEM) campaign of the 27–28 January 1992 substorm event using four different models: the AMIE technique, the IZMIRAN electrodynamic model (IZMEM), the Weimer ionospheric convection model, and the three-dimensional global fluid simulations. The global simulation model used by Winglee *et al.* [1997] is an independent global MHD model. They found that there is a significant disparity in the magnitudes of the cross-polar cap potential predicted by the different models. The AMIE model predicts the lowest potential, followed by the Weimer model, IZMEM, and the global MHD models. The typical factor between the highest and lowest is between 1.5 and 3. The relative change in the magnitude of the cross-polar cap potential is about the same for the different models. More recently, with another independent global MHD model, Raeder *et al.* [2001] reported that the polar cap potential for the 24 November 1996 substorm event is about twice that of the potential derived from AMIE model. It is noted that at some time intervals, the field aligned current is of similar magnitude for the two models. It appears that the discrepancy in the ionospheric conductances cause the discrepancy in the potential values [Raeder *et al.*, 2001].

[32] Why do global MHD models give higher polar cap potential than those derived from semiempirical models for some substorm events? It is still under investigation and needs further work. Our speculation is that this is due to the absence of realistic ring current effects in the global MHD models. With long period of strong southward IMF, (for example, the Wind satellite shows more than 7 hour (from 0500 to 1200 UT) of southward B_z greater than 10 nT on 10 January 1997), the simulation shows that the tail lobe density decreases in the near-Earth region. The region 2 current in the ionosphere that is closed by the westward

ring current is not well developed to feed back to the magnetosphere and maintain enough density level in the lobe. Lu *et al.* [1998] show observations of large ring current energy injection (around 300 GW) during the time period of interest. Low lobe density will have a direct effect on the precipitating electron flux derived from the equations (5), (7), and (8). The precipitating electron flux is proportional to the density at the inner boundary of magnetosphere model. The ionospheric Pedersen and Hall conductance derived from equations (2) and (3) is small when the precipitating electron flux is small. Actually, during the time period studied for the 10 January 1997 event the simulated maximum total Hall conductance is less than 10 mhos. With reasonable magnitude of the field-aligned current and insufficient ionospheric conductance, the resulting ionospheric potential is high. Therefore the abnormal high ionospheric electric potential is due to the absence of the ring current in the MHD model. A better ionospheric conductance model might also help to remedy this problem. We agree that the results presented here can be improved when global MHD model resolves this problem and that will be the focus of our future work.

5. Summary

[33] In this paper, we have presented a model to calculate the perturbed magnetic field at magnetometer sites from the output of the global MHD LFM code. The model uses the computed ionospheric current density distribution and the height dependence of the electrojet (determined by the energy of precipitating electrons) to calculate the perturbed magnetic field by implementing Biot-Savart's law. By applying it to 10 January 1997 magnetic storm event we calculated the perturbed magnetic field for four stations and compared them with observation from the magnetometers. The comparison shows reasonable agreement between observations and simulations. The model including the current layer height dependence on the precipitating electron energy reduces by 10% the error compared to the model with a fixed current sheet height. The limitations of the global MHD model in calculating ground observed perturbed magnetic field were also discussed. This model therefore expands the capability of the global MHD simulation to simulate individual ground magnetometer.

[34] Although the model including the height dependence of current sheet layer can improve the calculation results, the magnitude of our calculation is still less than the observations in active periods. We expect that predictions of empirical quantities will be improved as the MHD models incorporate realistic ring current model and better ionospheric conductance model. We will use this model with higher-resolution MHD runs. Also, we will improve our model for stations outside the polar cap boundary by including the effect of the parallel currents that may have a stronger influence compared to stations within the polar cap where opposing parallel currents have a tendency to cancel each other's contribution to the magnetic field. The ground magnetic field perturbations studied in this paper are caused by the solar wind density variations. In the future, in order to differentiate between solar wind velocity and density as drivers of magnetospheric response, we will simulate several events that have solar wind pressure changes for which

some are dominated by the solar wind density changes and others caused by changes in the solar wind velocity.

[35] **Acknowledgments.** The Wind satellite data were used courtesy of R. P. Lepping and K. W. Ogilive. Magnetometer data for Sondre Stromfjord was provided by Peter Stauning. Magnetometer data for Iqaluit was provided by Louis J. Lanzerotti. Magnetometer data for Rankin Inklet was provided by John Olson. We thank Ted Rosenberg and Dan Detrick for pointing us to the data source. Scientific computations were performed on ORIGIN2000 at the National Computational Science Alliance (NCSA), University of Illinois at Urbana-Champaign. This work was supported in part by the ISTP program NAG-51101 sponsored by NASA, NSF grants ATM-0003188, ATM-0001676 and NCSA grant MCA01S003N. The authors thank the referees for the valuable inputs.

[36] Janet G. Luhmann thanks Lee F. Bargatze and another referee for their assistance in evaluating this paper.

References

- Fedder, J. A., and J. G. Lyon, The solar wind-magnetosphere-ionosphere current-voltage relationship, *Geophys. Res. Lett.*, **8**, 880, 1987.
- Fedder, J. A., J. G. Lyon, S. P. Slinker, and C. M. Mobarry, Topological structure of the magnetotail as function of interplanetary magnetic field and with magnetic shear, *J. Geophys. Res.*, **100**, 3613, 1995a.
- Fedder, J. A., S. P. Slinker, J. G. Lyon, and R. D. Elphinstone, Global numerical simulation of the growth phase and the expansion onset for substorm observed by Viking, *J. Geophys. Res.*, **100**, 19,083, 1995b.
- Fukushima, N., Generalized theorem for no ground magnetic effect of vertical currents connected with Pedersen currents in the uniform conducting ionosphere, *Rep. Ionos. Space Res. Jpn.*, **30**, 35, 1976.
- Goodrich, C. C., M. Wiltberger, R. E. Lopez, K. Papadopoulos, and J. G. Lyon, An overview of the impact of the January 10–11, 1997 magnetic cloud on the magnetosphere via global MHD simulation, *Geophys. Res. Lett.*, **25**, 2537, 1998a.
- Goodrich, C. C., M. Wiltberger, R. E. Lopez, K. Papadopoulos, and J. G. Lyon, Global MHD Simulations of Actual Magnetospheric Substorm Events, *Substorms-4*, edited by S. Kokubun and Y. Kamide, p. 645, Terra Sci., Tokyo, Japan, 1998b.
- Gurevich, A. V., N. D. Borisov, and G. M. Milikh, *Physics of Microwave Discharges, Artificially Ionized Regions in the Ionosphere*, Gordon and Breach, New York, 1997.
- Jordanova, V. K., R. B. Torbert, R. M. Thorne, H. L. Collin, J. L. Roeder, and J. Foster, Ring current activity during the early Bz < 0 phase of the January 1997 magnetic cloud, *J. Geophys. Res.*, **104**, 24,895, 1999.
- Kisabeth, J. L., and G. Rostoker, Modelling of the three-dimensional current systems associated with magnetospheric substorms, *Geophys. J. R. Astron. Soc.*, **49**, 655, 1977.
- Lopez, R. E., M. Wiltberger, J. G. Lyon, and C. C. Goodrich, MHD simulations of the response of high-latitude potential patterns and polar cap boundaries to sudden southward turning of the interplanetary magnetic field, *Geophys. Res. Lett.*, **26**, 967, 1999.
- Lu, G., et al., Global energy deposition during the January 1997 magnetic cloud event, *J. Geophys. Res.*, **103**, 11,695, 1998.
- Milikh, G. M., et al., Modeling riometer observations of ionospheric absorption during substorms, *Geophys. Res. L.*, **28**, 487, 2001.
- Mobarry, C. M., J. A. Fedder, and J. G. Lyon, Equatorial plasma convection from global simulations of the Earth's magnetosphere, *J. Geophys. Res.*, **101**, 7859, 1996.
- Papadopoulos, K., C. Goodrich, M. Wiltberger, R. Lopez, and J. G. Lyon, The Physics of Substorms as revealed by ISTP, *Phys. Chem. Earth C*, **24**(1–3), 189, 1999.
- Raeder, J., et al., Global simulation of the Geospace Environment Modeling substorm challenge event, *J. Geophys. Res.*, **106**, 381, 2001.
- Rees, M. H., *Physics and Chemistry of the Upper Atmosphere*, Cambridge Univ. Press, New York, 1989.
- Robinson, R. M., R. R. Vondrak, K. Miller, T. Dabbs, and D. A. Hardy, On calculating ionospheric conductivities from the flux and energy of precipitating electrons, *J. Geophys. Res.*, **92**, 2565, 1987.
- Slinker, S. P., J. A. Fedder, B. A. Emery, K. B. Baker, D. Lummerzheim, J. G. Lyon, and F. J. Rich, Comparison of global MHD simulations with AMIE simulations for the events of May 19–20, 1996, *J. Geophys. Res.*, **104**, 28,379, 1999.
- Wiltberger, M., T. I. Pulkkinen, J. G. Lyon, and C. C. Goodrich, MHD simulation of the magnetotail during the December 10, 1996, substorm, *J. Geophys. Res.*, **105**, 27,649, 2000.
- Winglee, R. M., V. O. Papitashvili, and D. R. Weimer, Comparison of the high-latitude ionospheric electrodynamics inferred from global simulations and semiempirical models for the January 1992 GEM campaign, *J. Geophys. Res.*, **102**, 26,961, 1997.

C. C. Goodrich, G. Milikh, K. Papadopoulos, X. Shao, and A. Sharma, Department of Astronomy, University of Maryland, College Park, MD 20742, USA. (xshcn@astro.umd.edu; milikh@astro.umd.edu; kp@astro.umd.edu; ccg@avl.umd.edu; ssh@astro.umd.edu)

P. N. Guzdar, Institute for Plasma Research, University of Maryland, College Park, MD 20742, USA. (guzdar@ipr.umd.edu)

J. G. Lyon and M. Wiltberger, Department of Astronomy, Dartmouth College, Hanover, NH 03755, USA. (wiltbemj@tinman.dartmouth.edu; lyon@tinman.dartmouth.edu)